High-Resolution Sea Surface Current Vector Field Inversion Based on Circular Scanning SAR

Xiaonan Yao, Xiaoqing Wang, Lixia Liu, Shubo Liu, Xiang Su, Haifeng Huang, and Zheng Lu, *Senior Member, IEEE*

***Abstract*—The Doppler scatterometer is an instrument used in real aperture radar in conjunction with a circular scanning antenna and has wide swath and multiangle characteristics. Many scholars have studied sea surface current vector field based on the use of the Doppler scatterometer. However, the existing methods directly use the phase difference of the spectrometer's echo to obtain the current vector field, and the resolution can be improved. This study proposes a high-resolution inversion method for ocean surface current fields based on circular scanning synthetic aperture radar (SAR). The current field is estimated by the proposed method based on the Doppler spectrum of the single complex image to realize high-resolution current vector field inversion. The current field inversion of circular scanning SAR is very sensitive to attitude and wind field errors. Accordingly, a model is established to study the influences of the main errors on Doppler shift estimation, and a global optimization method is proposed to realize high-precision current velocity inversion and synchronous error estimation. The effectiveness of this method is verified by using airborne circular scanning SAR data.**

***Index Terms*—Circular scanning synthetic aperture radar (SAR), Doppler shift, least squares, sea surface current velocity.**

I. Introduction

THE ocean current is a critical ocean dynamic parameter that is linked to human activities [1]. Ocean currents play a significant role in the exchange of materials and energy and impact global climate change. Furthermore, the inversion of ocean currents facilitates the development of offshore oil and gas fields and the management of fishery resources. To comply with the data requirements of the survey report on oceanic variables by the European contribution to the Global Ocean Observing System [2], the two most critical components are sea surface current velocity and direction. Accurate measurement and monitoring of these parameters are, therefore, vital to investigating and monitoring ocean currents.

Currently, the ocean current field is mainly detected using field measurements and radar technologies. *In situ* current measuring equipment, such as current meters and drift buoys [3], [4], are used for measurements at discrete points, and radar technology, including shore-based radar, satellite altimeters, Doppler scatterers, and synthetic aperture radar (SAR), enables wide-area observations. X-band and high-frequency ground wave radar are examples of shore-based radar that can measure currents in near-shore areas but are inadequate for global observations [5], [6], [7], [8], [9]. Satellite altimeters estimate geostrophic currents by measuring sea surface height using the balance between the Coriolis force and the pressure force [10], [11]. However, altimeters are only suitable for measuring large-scale geostrophic currents and do not reflect other sea surface currents. For measuring the current field, SAR also plays a significant role. There are two commonly used methods for utilizing SAR data for current field measurements: Doppler centroid analysis (DCA) and along-track interferometry (ATI). DCA can only calculate the line-of-sight (LOS) velocity component of the sea surface current and ignore direction values; correspondingly, it is suitable for single-antenna SAR data processing [12]. The ATI method uses interference phases to achieve high-resolution measurements of the sea surface current field, which is one of the hottest methods for measuring the current field at present [13], [14]. However, the ATI method demands complex equipment and requires SAR data from at least two antennas. SAR satellites, such as Sentinel-1 and Envisat, can obtain high-resolution radial velocity measurements of the ocean surface, but their relatively narrow swath limits their use for global observations.

As compared to SAR, Doppler scatterometers have the advantage of multiangle and broad swath properties [15], [16]. When the Doppler scatterometer moves forward, its antenna continues to scan in a circular pattern; thus, it can revisit the same area many times from different directions within a short time to retrieve the sea surface current vector field. Therefore, Doppler scatterometers, such as pencil-beam rotating scatterometer [17], [18], [19], [20], [21], [22], [23] and sector-beam rotating scatterometer [24], [25], are proposed to measure sea surface velocity and direction. Currently, the inversion of the current vector field by the Doppler scatterometer has been verified by airborne data [20]. This method was used to estimate the current field based on the

Manuscript received 7 April 2023; revised 5 June 2023; accepted 29 June 2023. Date of publication 5 July 2023; date of current version 21 July 2023. This work was supported in part by the National Natural Science Foundation of China under Grant 41976174 and Grant 62071499, and in part by the Introduced Innovative R&D Team project of the Pearl River Talent Recruitment Program (2019ZT08X751). *(Corresponding author: Xiaoqing Wang.)*

Xiaonan Yao and Haifeng Huang are with the School of Electronic and Communication Engineering, Sun Yat-sen University, Shenzhen 518107, China (e-mail: yxnooo1@163.com; huanghaifeng@mail.sysu.edu.cn).

Xiaoqing Wang is with the School of Electronic and Communication Engineering, Sun Yat-sen University, Shenzhen 518107, China, and also with Pengcheng Laboratory, Shenzhen 518000, China (e-mail: wangxq58@mail.sysu.edu.cn).

Lixia Liu, Shubo Liu, and Xiang Su are with the China Academy of Space Technology (Xi'an), Xi'an 710100, China (e-mail: liulixia_504@163.com; liushubo163@163.com; gabriel1861@163.com).

Zheng Lu is with the China Academy of Space Technology, Beijing 100094, China (e-mail: lvzheng_cast@163.com).

Digital Object Identifier 10.1109/JSTARS.2023.3292613

phase difference of successive radar signals; correspondingly, its resolution depends on the beam's footprint. Therefore, the resolution of this method applied to the satellite platform is poor. The Sea Surface Kinesthetics Multiscale project of the European Space Agency [21], [22], [23] is built around a Ka-band pulsed radar that uses the phase difference of consecutive pulse returns to measure the LOS velocity of ocean surface targets. Although its resolution in the range direction is high, its azimuth resolution is limited to 6 km for Doppler.

The working mode of the circular scanning SAR is like that of a sector-beam rotating Doppler scatterometer, but the imaging resolution is improved by imaging processing. The circular scanning SAR is initially used for scene matching in the terminal guidance of missiles. In 2015, the National Aeronautics and Space Administration launched the soil moisture active and passive satellites equipped with a circular scanning antenna to detect global soil moisture [26]. Circular scanning SAR has been applied to the inversion of sea surface current field [27]. Pan et al. [27] assumed that the entire mapping area was a uniform current field and finally obtained an average value for the entire area rather than current vector field. Moreover, the existing methods use directly the phase difference of the echo to obtain the current vector field, and the resolution is not very high.

In this study, we propose a method for estimating the sea surface current vector field using circular scanning SAR. Unlike the methods based on echo phase differences, this method can retrieve a wide area of sea surface vector current field from multicycle echo data via a single antenna with significantly improved current field resolution. In Section II, we elaborate on the retrieval of the sea surface current vector field based on circular scanning SAR. Specifically, we extract the Doppler shift from different scanning angles and consider the Doppler frequency shift caused by attitude and wind field errors in circular scanning SAR to accurately estimate the sea surface current vector field. The high-precision current field inversion is achieved using a global optimization least squares method. In Section III, we evaluate and confirm the approach using airborne circular scanning SAR data. In Section IV, we discuss the applicability of this method, including the limitations of circular scanning SAR systems and the impact of environmental factors on the results. Finally, Section V conclude this article.

II. Sea Surface Current Vector Field Inversion of Circular Scanning SAR

A. Doppler Shift of Circular Scanning SAR for Ocean Surface

Fig. 1 presents the working schematic of circular scanning SAR. As the antenna moves forward along the *X*-axis, it rapidly and uniformly scans the imaging region on the ground, creating an almost annular area. Overlapping numerous annular areas forms a wide swath.

The Doppler frequency of the echo signal is affected by the relative motion between the circular scanning SAR platform and the sea surface, implying that the sea surface current field can be retrieved by using the Doppler shift. However, due to the complexity of ocean motion and the specialty of circular scanning SAR for ocean imaging, the Doppler shift f_{dc} in SAR

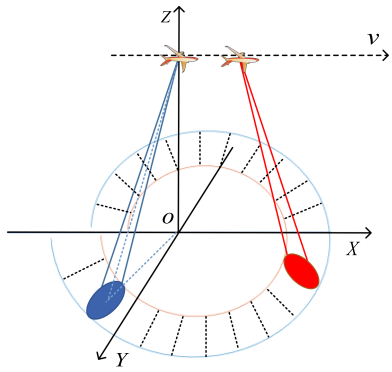

Fig. 1. Schematic of circular scanning SAR.

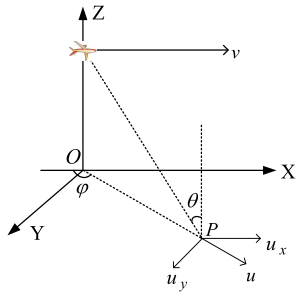

Fig. 2. Schematic of the geometric relationship between current and radar.

ocean data often comprises the following components:

$$f_{\mathrm{dc}} = f_{\mathrm{dc}}^{\mathrm{phys}} + f_{\mathrm{dc}}^{\mathrm{ng}} + \Delta f_{\mathrm{dc}} \tag{1}$$

where $f_{\mathrm{dc}}^{\mathrm{phys}}$ is a geophysical term resulting from ocean wave and current, $f_{\mathrm{dc}}^{\mathrm{ng}}$ represents nongeophysical biases caused by satellite orbit and attitude parameters, and Δf_{dc} denotes the residual error in data processing. Therefore, $f_{\mathrm{dc}}^{\mathrm{ng}}$ can be expressed as

$$f_{\mathrm{dc}}^{\mathrm{ng}} = f_r + \Delta f_r \tag{2}$$

where f_r represents the Doppler shift caused by platform motion and antenna rotation, whereas Δf_r denotes the residual Doppler shift caused by platform attitude errors.

One of our primary concerns pertains to the inclusion of the wind-driven component in the LOS direction of sea surface Doppler velocity. This component comprises the Ekman current, driven by surface wind stress, as well as the Stokes drift and wind-wave motions induced by the Bragg wave and the long-wave orbital velocity. Hence, $f_{\mathrm{dc}}^{\mathrm{phys}}$ can be decomposed into two components, namely

$$f_{\mathrm{dc}}^{\mathrm{phys}} = f_c + f_{\mathrm{wd}} \tag{3}$$

where f_c and f_{wd}, respectively, denote the ocean current and the wind-driven induced Doppler centroid (DC) variations.

Based on the geometric relationship between the ocean current and the radar platform, as depicted in Fig. 2, f_c at the target location P can be mathematically represented as

$$f_c = \frac{2}{\lambda}\left(-u_x \cos\varphi \sin\theta + u_y \sin\varphi \sin\theta\right)$$

$$= -\frac{2\cos\varphi\sin\theta}{\lambda}u_x + \frac{2\sin\varphi\sin\theta}{\lambda}u_y$$
$$= f'_{ux}\cdot u_x + f'_{uy}\cdot u_y \tag{4}$$

where u_x and u_y denote the current's azimuth direction and range direction velocity components, respectively. $\mathbf{u} = u_x\mathbf{x} + u_y\mathbf{y}$ is the velocity vector of the current field, $\mathbf{x}$ and $\mathbf{y}$ are unit vectors of the *X* and *Y* axes, respectively. λ is the electromagnetic wavelength, θ is the incident angle, and φ is the azimuth angle of the incident beam, i.e., the angle between the beam incident plane and the orbital plane.

In this equation, u_x and u_y represent the velocity components of the current field, respectively, in the azimuth and range directions. Meanwhile, $\mathbf{u} = u_x\mathbf{x} + u_y\mathbf{y}$ is the velocity vector of the current field, $\mathbf{x}$ and $\mathbf{y}$ are unit vectors of the *X* and *Y* axes, respectively. λ is the electromagnetic wavelength, θ is the incident angle, and φ is the azimuth angle of the incident beam, i.e., the angle between the beam incident plane and the orbital plane. It is important to note that in this discussion, we assume the counterclockwise rotation of the antenna. As illustrated in Fig. 2, an azimuth angle of 0° is applicable when the antenna points in the opposite flight direction, whereas for an antenna pointing in the flight direction, an azimuth angle of 180° applies. This assumption is made without any loss of generality.

As a result, the following equation represents the Doppler shift:

$$f_{dc} = f_c + f_{wd} + f_r + \Delta f_r + \Delta f_{\mathrm{dc}}. \tag{5}$$

The purpose of this study is to separate f_c from f_{dc} and extract the ocean current vector image. Specifically, the study aims to accurately estimate the relevant variables and eliminate the residual Doppler shift and wind-driven component. These eliminations are necessary to ensure high-precision data.

1) Nongeophysical Biases Model: The accuracy of current field estimation is affected by nongeophysical biases. These biases include the Doppler shift caused by platform motion and attitude errors. The Ku-band radar has a sea surface current speed measurement precision of 5 cm/s, which requires a slant range error of less than 20 m and an attitude angle error of less than 0.001° [17]. It is clear that the slant range error and attitude angle error significantly impact the estimation; hence, it is necessary to consider these errors when estimating the current field.

According to Yao et al. [28], assuming that Δf_r is caused by the slant range error ΔR, pitch error $\Delta\alpha$, roll error $\Delta\beta$, and yaw error $\Delta\gamma$, it can be expressed as

$$\Delta f_r = f_{\Delta R} + f_{\Delta\alpha} + f_{\Delta\beta} + f_{\Delta\gamma} \tag{6}$$

where $f_{\Delta R}, f_{\Delta\alpha}, f_{\Delta\beta}$, and $f_{\Delta\gamma}$, respectively, denote the Doppler shift caused by slant range error ΔR, pitch error $\Delta\alpha$, roll error $\Delta\beta$, and yaw error $\Delta\gamma$.

In addition, Yao et al. [28] establish a correlation between the slant range error, attitude angle error, and residual Doppler shift. This correlation means that when the errors are small enough, Δf_r can be approximated as a linear superposition of the four errors at different azimuth angles

$$\Delta f_r(\varphi) \approx \left(f'_{\Delta R}(\varphi)\cdot\Delta R + f'_{\Delta\alpha}(\varphi)\cdot\Delta\alpha + f'_{\Delta\beta}(\varphi)\cdot\Delta\beta + f'_{\Delta\gamma}(\varphi)\cdot\Delta\gamma\right) \tag{7}$$

where $f'_{\Delta R}(\varphi)$, $f'_{\Delta\alpha}(\varphi)$, $f'_{\Delta\beta}(\varphi)$, and $f'_{\Delta\gamma}(\varphi)$ are the expressions of $f_{\Delta R}(\varphi)$, $f_{\Delta\alpha}(\varphi)$, $f_{\Delta\beta}(\varphi)$, and $f_{\Delta\gamma}(\varphi)$ after the exclusion of the unknowns ΔR, $\Delta\alpha$, $\Delta\beta$, and $\Delta\gamma$ at different azimuth angles, respectively.

2) Doppler Shift Caused by Wind-Driven Components: Precisely determining and subtracting the wind-driven contribution is essential for accurately deducing sea surface currents from SAR Doppler data. Removing the contribution is difficult, and it is described as one of the biggest challenges in the current SAR recovery process. The Doppler shift caused by the wind-driven component f_{wd} can be decomposed into three components

$$f_{\mathrm{wd}} = f_E + f_S + f_{wv} \tag{8}$$

where f_E is the component of Ekman current induced by local wind stress at the surface, and f_S is the component of Stokes drift and wind-wave-induced motions. The term f_{wv} includes the phase speed of the Bragg wave and the correlation between backscatter variation and long-wave orbital velocities. However, it does not consider the Doppler shift resulting from actual water mass transport (current), although it does cause a Doppler shift in the radar measurements.

Accurate estimation of f_{wv} is extremely important. This affects many current measurement techniques and sensors: SAR, Doppler scatterometer [20], airborne, spaceborne, and tower-based [29] radars. The component f_{wv} was investigated by several authors. For instance, Thompson [30] showed that not only do the widths of the Doppler spectra broaden owing to the motion of the long waves, but also a centroid shift is produced from the Bragg frequency. The author also showed that this shift is maximized at lower incidence angles and higher radar frequencies. This means that even in the absence of currents, the radar measures a Doppler shift from the Bragg phase speed. Furthermore, this DC shift contributes a significant amount (∼30% of the wind speed) to the Doppler velocity measured by SAR [12]; this contribution is often larger than the current we want to retrieve.

The sum of the Ekman and Stokes components is commonly referred to as the "drift current" and can be parameterized in the wind speed. This phenomenon was previously investigated and discussed in [31] and [32]. The reported magnitudes ranged between ∼1% and ∼4% of the wind speed, and the direction varied between 0° and 45°, depending on wind speed, fetch, sea state, and stratification.

The CDOP model is an empirical geophysical model function that estimates the Doppler shift of wind-driven components. Researchers [12], [33] demonstrated that the DCA, the difference between the observed DC and the geometric Doppler shift, has a distinct geophysical signature based on the examination of the C-band ENVISAT/advanced SAR data at a worldwide scale. This signature has been shown by Mouche et al. [34] to be correlated with the global wind field. The CDOP model predicts the Doppler shift of the C-band at both VV and HH polarizations as a function of wind speed, radar incidence angle, and wind direction relative to the radar's look direction. Thus, the CDOP

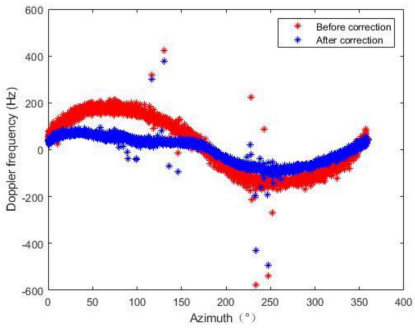

Fig. 3. Comparison before and after CDOP correction.

model can be described as follows:

$$f_{CDOP} = f_{CD}\left(\theta, u_{10}, \phi, pol\right) \tag{9}$$

where f_{CDOP} denotes the Doppler shift of wind-driven components, ϕ represents the wind direction relative to the radar look direction, u_{10} is the wind speed measured 10 m above the ground, θ is the incidence angle, and pol can be either VV or HH. As a result, f_{CDOP} can substitute for f_{wd}.

The KuDop GMF was proposed by scaling the CDOP model to the Ku-band with a scale factor of approximately 2.6 (e.g., 13.6/5.3) [35]. Based on the similarities between the Envisat C-band CDOP model and the X-band wave-mill proof-of-concept airborne data, Martin et al. [36] demonstrated the validity of carrier frequency scaling by examining the similarities between the Envisat C-band CDOP model and the X-band wave-mill proof-of-concept airborne data. Theoretical considerations [37] support this finding.

However, $\hat{f} = f_{dc} - k_f \cdot f_{CDOP}$ is that the shift error caused by wind is subtracted from the estimated Doppler shift, where k_f is frequency scaling factor. Our calculations, using actual airborne circular scanning SAR data shown in Fig. 3, suggest that no discernible cosine change is observed when the frequency shift error induced by the wind and wave is subtracted from the estimated Doppler shift. In Fig. 3, the abscissa represents the azimuth angle from 0° to 360°, whereas the ordinate represents the DC frequency that changes with the azimuth. The Ku-band SAR data were acquired on January 11, 2016, at 00:00 UTC from the Jiaodong Peninsula, China. Additional information can be found in Section III-A. Speculatively, the application of the CDOP model to the Ku-band, based solely on frequency scaling, may result in significant errors. To compensate for the errors generated by the Ku-band model, a correction term f_m needs to be added, which can be expressed as

$$f_m = \text{abs}\left(\cos\left(\varphi - \phi\right)\right)\Delta m = f'_m \cdot \Delta m \tag{10}$$

where Δm is the undetermined correction factor.

Furthermore, wind errors, including speed and direction, can significantly affect current retrievals, leading to degraded performance, especially when considering wind direction error [38]. In addition, current direction error is more susceptible to wind errors than current velocity error. Therefore, this study focuses on the impact of wind direction error $\Delta wind$ on our calculations.

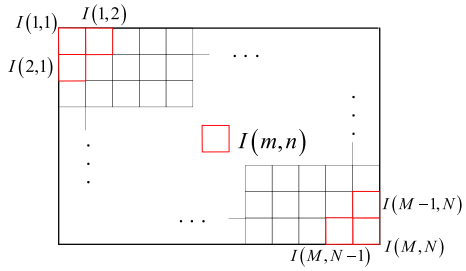

Fig. 4. Schematic of SAR image blocking.

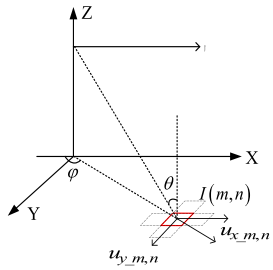

Fig. 5. Current field diagram of subblock image.

Thus, (8) can be expressed as follows:

$$f_{wd} = k_f \cdot f_{CDOP} + f_w + f_m \tag{11}$$

$$f_w = \frac{\partial f_{CDOP}}{\partial wind}\Delta wind = f'_w \cdot \Delta wind. \tag{12}$$

Therefore, (5) can be expressed as

$$\begin{aligned} f_{dc} = {} & f_c + f_r + f_{\Delta R} + f_{\Delta\alpha} + f_{\Delta\beta} + f_{\Delta\gamma} + k_f \cdot f_{CDOP} \\ & + f_w + f_m + \Delta f_{dc}. \end{aligned} \tag{13}$$

That is

$$\begin{aligned} \hat{f} = {} & f_{dc} - k_f \cdot f_{CDOP} - f_r \\ = {} & f'_{ux} \cdot u_x + f'_{uy} \cdot u_y \\ & + f'_{\Delta R} \cdot \Delta R + f'_{\Delta\alpha} \cdot \alpha + f'_{\Delta\beta} \cdot \beta \\ & + f'_{\Delta\gamma} \cdot \gamma \cdot + f'_w \cdot \Delta wind + f'_m \cdot \Delta m + \Delta f_{dc}. \end{aligned} \tag{14}$$

B. Sea Surface Current Field Estimation Method Based on Global Weighted Least Squares

The circular scanning SAR data undergoes deramping and match-filtering to obtain a single view multiple (SLC) image [39]. After deramping, the Doppler shift caused by platform motion f_r is canceled [28]. The Doppler shift $\Delta f_{dc} = f_{dc} - f_r$ is then estimated using an optimal estimator method [40], [41].

To estimate a two-dimensional sea surface current vector field, we divided the entire image into *M* rows and *N* columns of subimages. As depicted in Fig. 4, each subimage can calculate the estimation result of a current vector field. In this case, the subimage located at row *m* and column *n* is expressed as $I(m, n)$.

Each subimage has the same along-track speed $u_{x\_m,n}$ and cross-track speed $u_{y\_m,n}$ of the sea surface current field at subimage $I(m, n)$, as shown in Fig. 5.

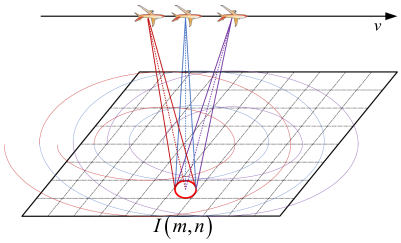

Fig. 6. Schematic of ocean current vector field.

For the entire image, the vector matrix of the 2-D current field can be obtained and expressed as

$$\mathbf{U_x} = \begin{bmatrix} u_{x\_1,1} & \cdots & u_{x\_1,N} \\ \vdots & \vdots & \vdots \\ u_{x\_M,1} & \cdots & u_{x\_M,N} \end{bmatrix} \tag{15}$$

$$\mathbf{U_y} = \begin{bmatrix} u_{y\_1,1} & \cdots & u_{y\_1,N} \\ \vdots & \vdots & \vdots \\ u_{y\_M,1} & \cdots & u_{y\_M,N} \end{bmatrix}. \tag{16}$$

Because circular scanning SAR has the characteristics of flying while scanning, the same area can be observed at different azimuth angles with k circle scanning data, that is, the subimage $I(m,n)$ can be irradiated several times, as shown in Fig. 6.

Therefore, we can obtain the Doppler shift estimation results of the $I(m,n)$ images $\hat{f}_{m,n}(\varphi)$ at different azimuth angles. After obtaining the Doppler shift, the following equation can be obtained:

$$\mathbf{F_{m,n}} = \mathbf{A_{m,n}} \times \mathbf{b_{m,n}} + \mathbf{N_{m,n}}. \tag{17}$$

In the subimage $I(m,n)$, $\mathbf{F_{m,n}}$ is the Doppler shift matrix after CDOP correction, $\mathbf{A_{m,n}}$ is the coefficient matrix, $\mathbf{b_{m,n}}$ is the matrix to be solved, and $\mathbf{N_{m,n}}$ is the noise matrix corresponding to the DC estimation error. To ensure the consistency of the noise term, each equation is normalized using the DC estimation accuracy $\delta_f(\varphi)$, defined as

$$\delta_f(\varphi) \approx 0.54 \frac{B_\eta(\varphi)^2}{PRF\sqrt{N_{\text{num}}}} \tag{18}$$

where $B_\eta(\varphi)$ is the Doppler bandwidth, N_{num} is the total number of points involved in the Doppler spectrum calculation.

$\mathbf{F_{m,n}}$, $\mathbf{A_{m,n}}$, and $\mathbf{b_{m,n}}$ are, respectively, expressed as (20) shown at the bottom of this page,

$$\mathbf{F_{m,n}} = \left[\frac{\hat{f}_{m,n}(\varphi_1)}{\delta_f(\varphi_1)}, \ldots, \frac{\hat{f}_{m,n}(\varphi_k)}{\delta_f(\varphi_k)} \right]^T \tag{19}$$

$$\mathbf{b_{m,n}} = \left[\Delta R \quad \Delta\alpha \quad \Delta\beta \quad \Delta\gamma \quad \Delta wind \quad \Delta m \quad u_{x\_m,n} \quad u_{y\_m,n} \right]^T. \tag{21}$$

Because there are several unknowns in $\mathbf{b_{m,n}}$, the least squares method requires more equations to obtain accurate estimation results. Fortunately, the slant range error and attitude errors of the system can be regarded as constant within several cycles of continuous revisit, and the wind field error can be regarded as a fixed value within a large range (such as tens of kilometers). That is, with the exception of ΔR, $\Delta\alpha$, $\Delta\beta$, $\Delta\gamma$, $\Delta wind$, and Δm, only $u_{x\_m,n}$ and $u_{y\_m,n}$ change with the subblock image. Therefore, $\mathbf{A_{m,n}}$ can be divided into two submatrices $\mathbf{A^1_{m,n}}$ and $\mathbf{A^2_{m,n}}$ according to whether it changes with the subblock image, which can be, respectively, expressed as (22) shown at the bottom of the next page,

$$\mathbf{A^2_{m,n}} = \begin{bmatrix} \frac{f'_{ux\_m,n}(\varphi_1)}{\delta_f(\varphi_1)} & \frac{f'_{uy\_m,n}(\varphi_1)}{\delta_f(\varphi_1)} \\ \vdots & \vdots \\ \frac{f'_{ux\_m,n}(\varphi_k)}{\delta_f(\varphi_k)} & \frac{f'_{uy\_m,n}(\varphi_k)}{\delta_f(\varphi_k)} \end{bmatrix}. \tag{23}$$

The overall matrix can be constructed, and the global optimization least squares can be calculated according to the following equation:

$$\mathbf{F} = \mathbf{A} \times \mathbf{b} + \mathbf{N}. \tag{24}$$

In the area where the wind field is regarded to have a constant value, $\mathbf{F}$ is the Doppler shift matrix after CDOP correction, $\mathbf{A}$ is the coefficient matrix, $\mathbf{b}$ is the matrix to be solved, and $\mathbf{N}$ is the noise matrix

$$\mathbf{F} = [\mathbf{F_{1,1}}; \ldots; \mathbf{F_{M,N}}] \tag{25}$$

$$\mathbf{A} = \begin{bmatrix} \mathbf{A^1_{1,1}} & \mathbf{A^2_{1,1}} & & & O \\ \vdots & & \ddots & & \\ \mathbf{A^1_{m,n}} & O & & \mathbf{A^2_{m,n}} & O \\ \vdots & & & \ddots & \\ \mathbf{A^1_{M,N}} & & O & & \mathbf{A^2_{M,N}} \end{bmatrix} \tag{26}$$

$$\mathbf{b} = [\Delta R \quad \alpha \quad \beta \quad \gamma \quad \Delta wind \quad \Delta m \quad u_{x\_1,1} \quad u_{y\_1,1} \quad \ldots \quad u_{x\_m,n} \quad u_{y\_m,n} \quad \ldots \quad u_{x\_M,N} \quad u_{y\_M,N}]^T. \tag{27}$$

The result can be obtained by the least squares method

$$\mathbf{b} = \left(\mathbf{A}^T\mathbf{A}\right)^{-1}\mathbf{A}^T\mathbf{F}. \tag{28}$$

Finally, we can rearrange $u_{x\_m,n}$ and $u_{y\_m,n}$ according to the positions of m and n to obtain the final results $\mathbf{U_x}$ and $\mathbf{U_y}$, respectively.

$$\mathbf{A_{m,n}} = \begin{bmatrix} \frac{f'_{\Delta R\_m,n}(\varphi_1)}{\delta_f(\varphi_1)} & \frac{f'_{\Delta\alpha\_m,n}(\varphi_1)}{\delta_f(\varphi_1)} & \frac{f'_{\Delta\beta\_m,n}(\varphi_1)}{\delta_f(\varphi_1)} & \frac{f'_{\Delta\gamma\_m,n}(\varphi_1)}{\delta_f(\varphi_1)} & \frac{f'_{w\_m,n}(\varphi_1)}{\delta_f(\varphi_1)} & \frac{f'_{m\_m,n}(\varphi_1)}{\delta_f(\varphi_1)} & \frac{f'_{ux\_m,n}(\varphi_1)}{\delta_f(\varphi_1)} & \frac{f'_{uy\_m,n}(\varphi_1)}{\delta_f(\varphi_1)} \\ \vdots & \vdots & \vdots & \vdots & \vdots & \vdots & \vdots & \vdots \\ \frac{f'_{\Delta R\_m,n}(\varphi_k)}{\delta_f(\varphi_k)} & \frac{f'_{\Delta\alpha\_m,n}(\varphi_k)}{\delta_f(\varphi_k)} & \frac{f'_{\Delta\beta\_m,n}(\varphi_k)}{\delta_f(\varphi_k)} & \frac{f'_{\Delta\gamma\_m,n}(\varphi_k)}{\Delta f(\varphi_k)} & \frac{f'_{w\_m,n}(\varphi_k)}{\delta_f(\varphi_k)} & \frac{f'_{m\_m,n}(\varphi_k)}{\delta_f(\varphi_k)} & \frac{f'_{ux\_m,n}(\varphi_k)}{\delta_f(\varphi_k)} & \frac{f'_{uy\_m,n}(\varphi_k)}{\delta_f(\varphi_k)} \end{bmatrix} \tag{20}$$

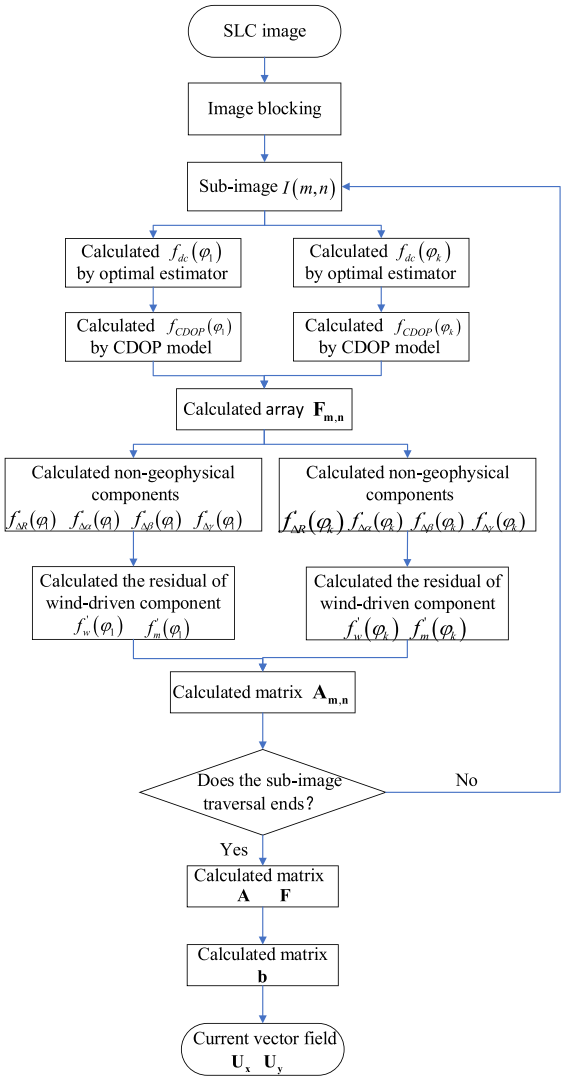

Fig. 7. Flowchart of current field inversion method based on global optimization least squares.

The flowchart of the current field inversion method based on the global optimization least squares is shown in Fig. 7.

III. Experimental Results and Analyses

A. Circular Scanning SAR Data

In this section, our primary focus is to verify the effectiveness of the proposed sea surface current field estimation method using real data from airborne circular scanning SAR. The datasets are SLC images from 23 circles obtained after deramping. These datasets were obtained on January 11, 2016 at 00:00 UTC from the Jiaodong Peninsula in China using an airborne circular scanning SAR. The scanning area was located at longitude: 123.5° E and latitude: 36.7° N. The circular scanning SAR system's key parameters are listed in Table I. As shown in Fig. 8, the imaging method of deramping was applied to compose 23 circles of echo data. The red box highlights several ships whose speeds are higher than the current field speed; all other areas (excluding the ships) represent sea surfaces. Fig. 9 is an enlarged

TABLE I
System Parameters of the Circular Scanning SAR

Parameters	Values
Range resolution	13.26 GHz
Platform speed	58 m/s
Platform flight height	3000 m
Antenna scanning rate	26 °/s
Pulse repetition frequency	4000 Hz
Looking angle of beam center	60°
Antenna beam width	4.7°
Polarization	HH

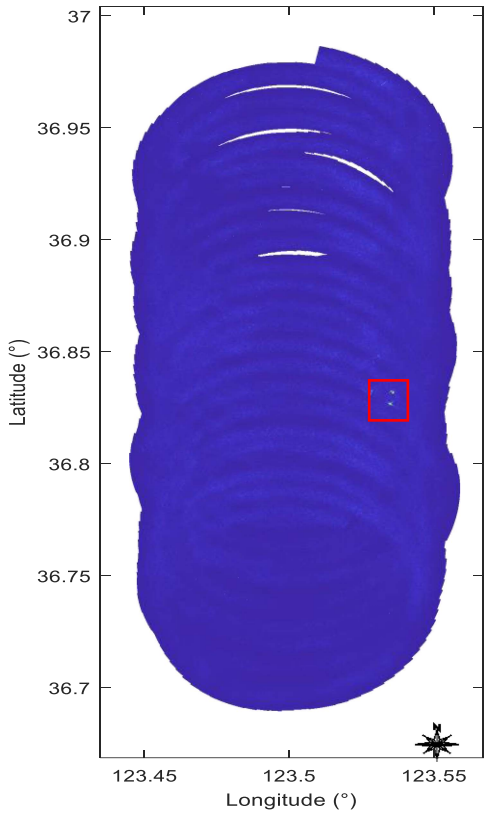

Fig. 8. Imaging results related to the SAR data of 23 circles.

$$\mathbf{A}^{\mathbf{1}}_{\mathbf{m,n}} = \begin{bmatrix} \frac{f'_{\Delta R\_m,n}(\varphi_1)}{\delta_f(\varphi_1)} & \frac{f'_{\Delta\alpha\_m,n}(\varphi_1)}{\delta_f(\varphi_1)} & \frac{f'_{\Delta\beta\_m,n}(\varphi_k)}{\delta_f(\varphi_1)} & \frac{f'_{\Delta\gamma\_m,n}(\varphi_1)}{\delta_f(\varphi_1)} & \frac{f'_{w\_m,n}(\varphi_1)}{\delta_f(\varphi_1)} & \frac{f'_{m\_m,n}(\varphi_1)}{\delta_f(\varphi_1)} \\ \vdots & \vdots & \vdots & \vdots & \vdots & \vdots \\ \frac{f'_{\Delta R\_m,n}(\varphi_k)}{\delta_f(\varphi_k)} & \frac{f'_{\Delta\alpha\_m,n}(\varphi_k)}{\delta_f(\varphi_k)} & \frac{f'_{\Delta\beta\_m,n}(\varphi_k)}{\delta_f(\varphi_k)} & \frac{f'_{\Delta\gamma\_m,n}(\varphi_k)}{\delta_f(\varphi_k)} & \frac{f'_{w\_m,n}(\varphi_k)}{\delta_f(\varphi_k)} & \frac{f'_{m\_m,n}(\varphi_k)}{\delta_f(\varphi_k)} \end{bmatrix} \tag{22}$$

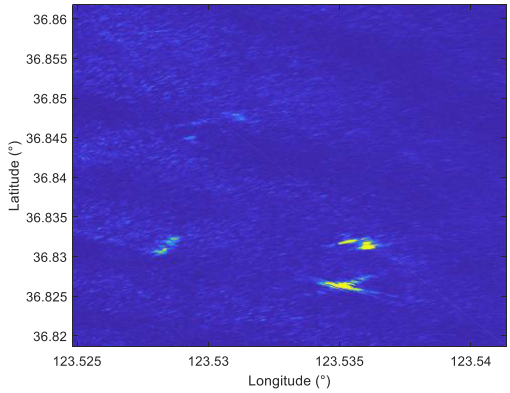

Fig. 9. Enlarged image of the red box in Fig. 8.

image of the red box. It shows the ships and the texture of the water.

The actual sea current velocity is measured by a ground-truth buoy located at 123.3014 E, 36.5157 N. The buoy measured the current velocity in this area at 0.56 m/s, and the current direction was 200°, with 0° indicating due north. Due to the synergy of the ocean in the current field, buoy data can be used to preliminarily evaluate the effectiveness of the proposed current field estimation method.

We acquired the wind field data at the test site and time (January 11, 2016, longitude: 123.5009° E, latitude: 36.72° N) by querying meteorological reanalysis data from the European Centre for Medium-Range Weather Forecasts website. The wind speed was determined to be 9.51 m/s, with the wind direction calculated as 7.005° south-east. As the experimental area was relatively small in our airborne experiment, we considered the wind field error to be fixed throughout the entire image.

B. Sea Surface Current Inversion

Following the steps proposed in Section II, we obtained the imaging results for each circle in the circular scanning SAR data and used the optimal estimator to obtain the 2-D Doppler shift results for each circle. We then calculated the CDOP frequency corresponding to each azimuth based on the supplied wind filed parameters and subtracted it from the estimated results. Next, we calculated each parameter in matrix A and performed the least squares calculation. Finally, we compared and analyzed the experimental results under six different conditions, where each condition considered different error terms, as shown in Table II.

1) Experiment 1: Experiment 1 does not consider any errors, and assumes that the estimated Doppler shift is caused by the current field u_x and u_y. Accordingly, (14) is expressed as

$$f_{dc} = f'_{ux} \cdot u_x + f'_{uy} \cdot u_y + \Delta f_{dc}. \tag{29}$$

In this case, the matrix to be solved $\mathbf{b_{m,n}}$ contains only $u_{x\_m,n}$ and $u_{y\_m,n}$. Based on the same process, the result is shown in Fig. 10.

2) Experiment 2: Experiment 2 only considered the nongeophysical term, that is

$$f_{dc} = f'_{ux} \cdot u_x + f'_{uy} \cdot u_y + f'_{\Delta R} \cdot \Delta R + f'_{\Delta\alpha} \cdot \Delta\alpha + f'_{\Delta\beta} \cdot \Delta\beta + f'_{\Delta\gamma} \cdot \Delta\gamma. \tag{30}$$

Based on the same process, the result is shown in Fig. 11.

3) Experiment 3: Experiment 3 considered the nongeophysical and wind-driven terms. That is, the CDOP model is considered based on experiment 2. Therefore, (14) was changed to

$$\hat{f} = f'_{ux} \cdot u_x + f'_{uy} \cdot u_y + f'_{\Delta R} \cdot \Delta R + f'_{\Delta\alpha} \cdot \Delta\alpha + f'_{\Delta\beta} \cdot \Delta\beta + f'_{\Delta\gamma} \cdot \Delta\gamma. \tag{31}$$

Based on the same process, the result is shown in Fig. 12.

4) Experiment 4: When the CDOP correction term f_w is not considered, (14) is expressed as

$$\hat{f} = f'_{ux} \cdot u_x + f'_{uy} \cdot u_y + f'_{\Delta R} \cdot \Delta R + f'_{\alpha} \cdot \alpha + f'_{\beta} \cdot \beta + f'_{\gamma} \cdot \gamma + f'_{w} \cdot \Delta wind + \Delta f_{dc}. \tag{32}$$

Based on the same process, the result is shown in Fig. 13.

5) Experiment 5: To demonstrate that our proposed method improves spatial resolution compared to previous methods and to verify its efficacy, we conducted experiment 5. This experiment estimated DC using the ACCC method without undergoing the imaging process of matched filtering. We also considered all the error terms used in experiment 6 and completed the calculation using the same inversion procedures. Fig. 14 shows the estimated current vector field as a result.

6) Experiment 6: When we considered all the mentioned error terms, we calculated them according to (14). Fig. 15 is the result of the estimated current vector field.

TABLE II
ERROR SETTINGS IN ABLATION EXPERIMENT

Experiment	Non-geophysical term	Wind-driven term	Wind direction error	Correction term	DC estimation method
1					Our method
2	√				Our method
3	√	√			Our method
4	√	√	√		Our method
5	√	√	√	√	ACCC before imaging
6	√	√	√	√	Our method

C. Experimental Analysis

Given the small radar coverage area, we can assume that the current velocity within this area is consistent. As such, the eastward velocity, northward velocity, and current velocity obtained from each experiment shown in Table III are the statistical values for this area. In this study, we use a histogram statistical method to calculate these values, taking the peak point of the speed histogram as the statistical value. This approach helps to avoid interference from outliers, such as ship speed, image middle, and image edge. For Table III, the velocity estimation errors and direction estimation errors are indicative of the difference between the estimation results and buoy data. Our proposed

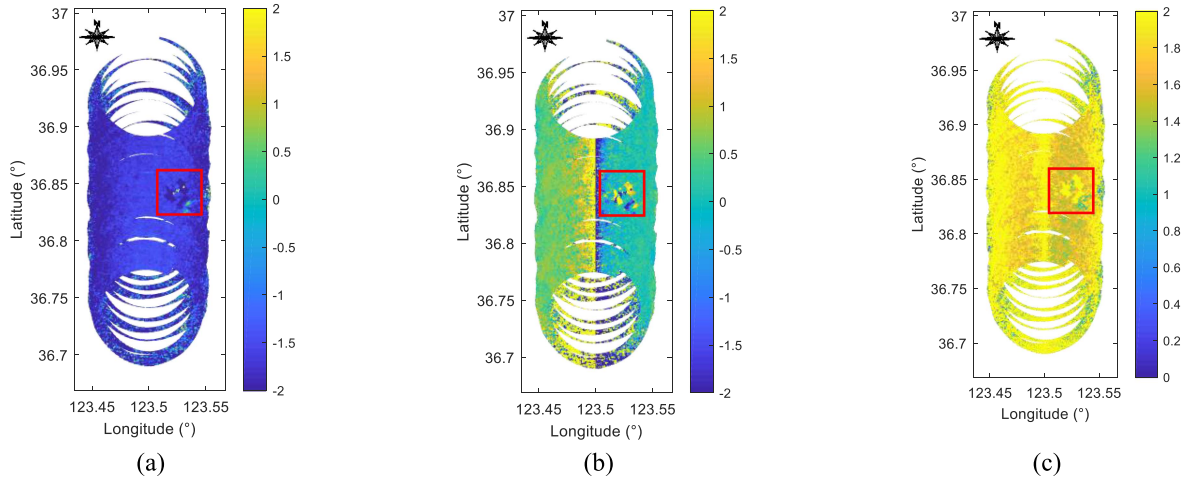

Fig. 10. Results of estimated current vector field in experiment 1: (a) Northward velocity, (b) eastward velocity, and (c) estimated results of the current vector field.

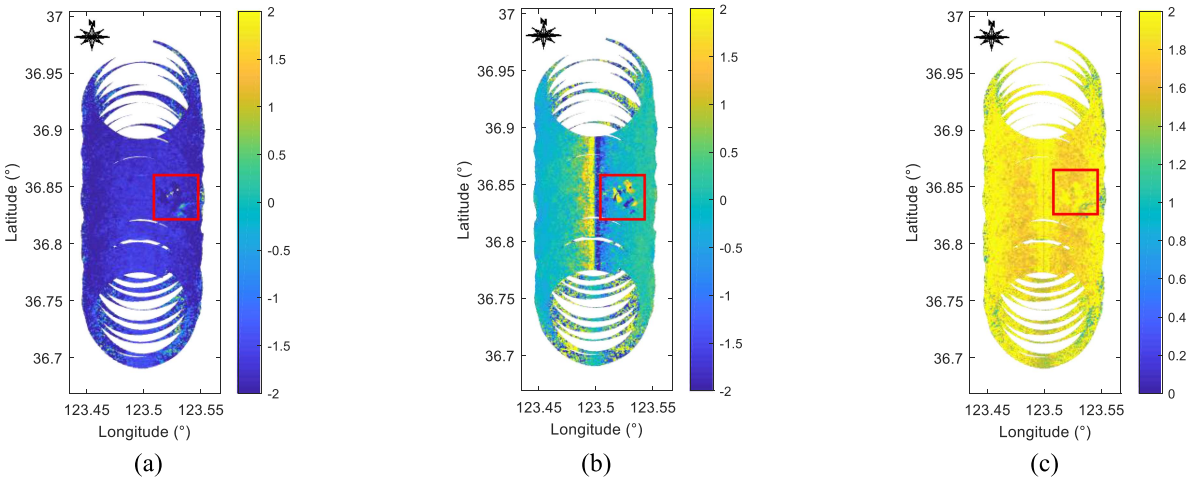

Fig. 11. Results of estimated current vector field in experiment 2: (a) Northward velocity, (b) eastward velocity, and (c) estimated results of the current vector field.

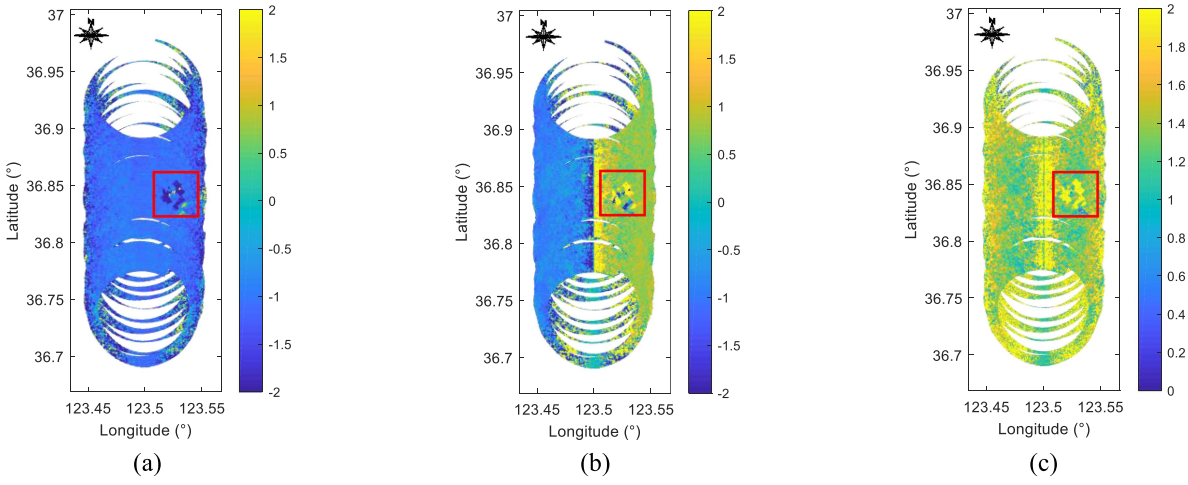

Fig. 12. Results of estimated current vector field in experiment 3: (a) Northward velocity, (b) eastward velocity, and (c) estimated results of the current vector field.

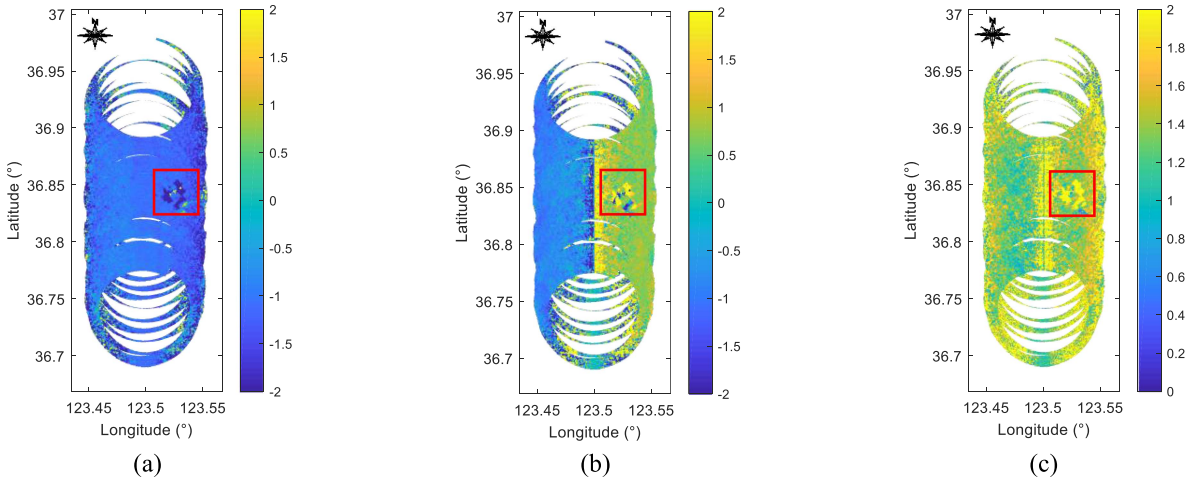

Fig. 13. Results of estimated current vector field in experiment 4: (a) Northward velocity, (b) eastward velocity, and (c) estimated results of the current vector field.

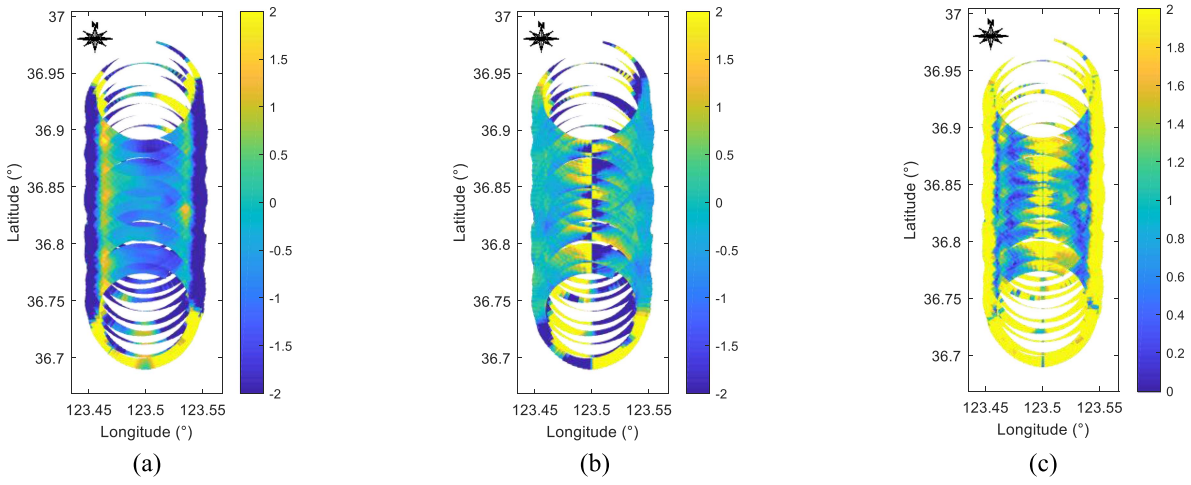

Fig. 14. Results of estimated current vector field in experiment 5: (a) Northward velocity, (b) eastward velocity, and (c) estimated results of the current vector field.

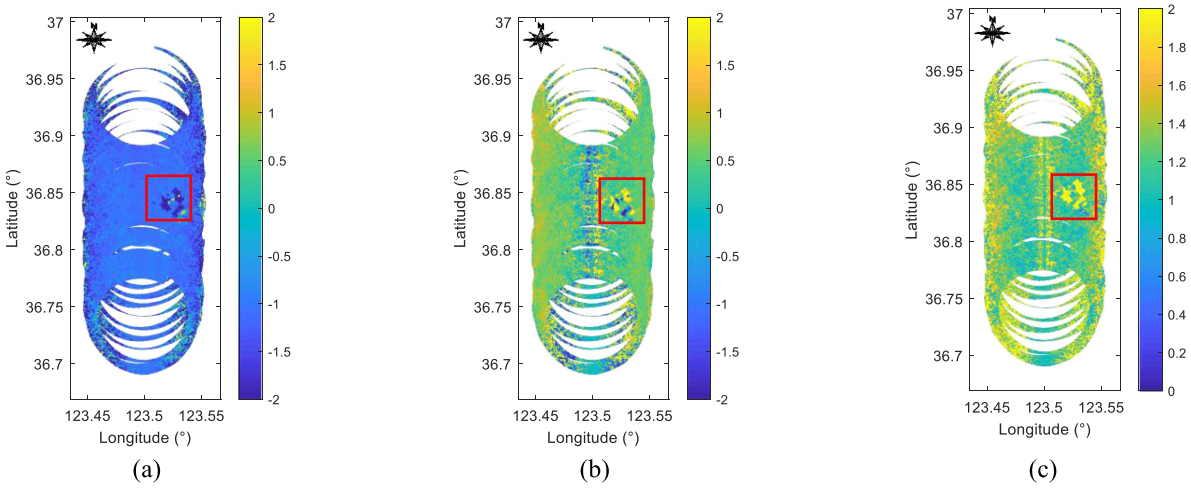

Fig. 15. Results of estimated current vector field in experiment 6: (a) Northward velocity, (b) eastward velocity, and (c) estimated results of the current vector field.

TABLE III
ESTIMATED RESULTS OF THE CURRENT FIELD

Experiment	Northward velocity	Eastward velocity	Current velocity	Velocity estimation error	Current direction	Direction estimation error
1	-1.52 m/s	90 m/s	61.7 m/s	61.14 m/s	269.03 °	69.03 °
2	-1.72 m/s	0.018m/s	1.77 m/s	1.21 m/s	180.61 °	19.39 °
3	-1.05 m/s	0.66 m/s	1.32 m/s	0.76 m/s	212.12 °	12.12 °
4	-1.04 m/s	0.78 m/s	1.27 m/s	0.71 m/s	216.73 °	16.73 °
5	-0.79 m/s	0.13 m/s	0.79 m/s	0.23 m/s	189.76 °	10.24 °
6	-0.68 m/s	0.21 m/s	0.63 m/s	0.07 m/s	203.16 °	3.16 °

method in experiment 6 demonstrates higher accuracy compared to the classic ACCC method used in experiment 5. The velocity error for experiment 6 is 0.07 m/s, and the direction error is 3.16°, which preliminarily verifies the feasibility of our proposed method.

By comparing experiment 5 with other experiments, it can be found that the spatial resolution of the current field inversion results we proposed is higher. Experiment 5 shows that the previous method has a lower spatial resolution, and the resolution of this method depends on the beam footprint. The azimuth resolution is limited to the size of the azimuth angle in the beam coverage area, whereas the range resolution is limited to the size of the beam coverage area. That is, the spatial resolution in Fig. 14 is about 110 m $\times$ 755 m. Our method is obtained through the optimal estimator method based on SLC images, and the obtained spatial resolution of the current field is 27.6 $\times$ 5.9 m. In addition, Fig. 9 shows that ships are present in the experimental area and are moving faster than the current velocity. Compared to Fig. 14, the current field results of the other five experiments can show the position of the ship, as shown in the red box. Therefore, without considering any errors, this method also significantly improves the spatial resolution of two-dimensional current field inversion. Moreover, compared with the results of experiment 5, the estimation error of experiment 6 is smaller, as shown in Table III. Therefore, taking into account the same error term, our proposed estimation method has more accurate estimation results than previous methods.

In order to improve the estimation accuracy of current vector fields (velocity and direction), we also considered various errors. As shown in Fig. 10(b), without considering any error terms, the eastward current field is in opposite directions on both sides of the flight direction. After considering the attitude errors, as shown in Fig. 11(b), the two sides of the eastward current field obviously tend to be consistent. This is because attitude errors are largely affected by azimuth angle, especially roll and yaw errors, which have a cosine relationship with azimuth angle. It is worth noting that due to the presence of forward-looking and backward-looking situations in antenna scanning of circular scanning SAR, in this case, the azimuth direction and range direction are severely coupled, so there is no reference to the position of the nadir.

The findings from experiments 3 and 4 demonstrate the inadequacies of using the CDOP frequency scaling method without considering correction terms, as illustrated in Figs. 12(b) and 13(b), which present opposing eastward velocity directions on either side of the flight path. Therefore, it is essential to consider the correction terms of the CDOP model to rectify the errors. After taking into account the correction term, the outcomes for the eastward current field have been rectified, as demonstrated in Fig. 15(b). In addition, according to Table III, the calculated error for experiment 6 is significantly lower than that of the preceding four experiments, which supports the notion that the estimated outcomes become more precise with the increase in the number of corrected errors.

The aforementioned experiments reveal significant values in both the middle and on the sides of the image. The large errors, particularly in the middle region, can be attributed to two primary reasons. First, due to the poor imaging resolution near the nadir, the current field inversion error is significant. Second, the condition number of $\mathbf{A_{m,n}}$ in (20) is excessively large, which happens as the azimuth angles of several observations in the vicinity of the nadir are too close, nearly 0°. Furthermore, there are two factors responsible for the significant error values observed on both sides of the image. The first reason is the record of scant data on either side of the image. The second factor is the proximity of azimuth angles in these regions to 90°. Consequently, the condition number of $\mathbf{A_{m,n}}$ is significantly large, leading to errors in the inversion values on both sides.

IV. DISCUSSION

This article uses comparative experiments with different methods to indirectly demonstrate the effectiveness of our method and the necessity of considering various factors through the continuity and self-consistency of the current field. The validity of the experimental results was also directly verified by the buoy data, but unfortunately, the buoy data in this experiment are limited. There is only one buoy near the experimental area, and the distance is relatively far, which leads to a certain lack of proof power for verification. In the future, we will conduct more measurements to further verify and improve our method.

Although circular scanning SAR has the advantage of a large and wide observation, its inherent principle leads to the use of forward-looking or backward-looking observations near the nadir. The azimuth resolution of circular scanning SAR during forward-looking and backward-looking observations is very poor. In addition, when multiple observations are made to invert the current field, the angle difference between the multiple observations is close to 0° or 180°, which can cause the matrix inversion step in the current field retrieval to have a too-large

matrix condition number. This results in significant inversion errors, so when using circular scanning SAR for large-scale current field observation, it is necessary to use other sensors to compensate for its observation defects in the nadir.

V. Conclusion

The sea surface current field is crucial and has a significant impact on global climatic change and human activities. Velocity and direction information are among the most valuable parameters in ocean research. Currently, the circular scanning radar is a popular research topic in ocean current vector field inversion due to its wide swath and multiangle advantages. Nevertheless, existing methods directly use the phase difference of the echo to obtain the current vector field, which results in relatively low resolution. To overcome this limitation and achieve high-resolution current field inversion, we propose a current vector field inversion method based on circular scanning SAR.

This method achieves high spatial resolution inversion by estimating the current field based on the Doppler spectrum of SLC images. Furthermore, the inversion process considers the impact of both attitude error and wind field error on the Doppler shift. The global optimization method is applied to achieve current field inversion and synchronization error estimation. We verified the effectiveness of this method using airborne circular scanning SAR data for current field inversion. Compared to the ACCC method, the estimation method based on SLC images has a higher spatial resolution and leads to a 28.5% improvement in the accuracy of current field estimation. In addition, we found that the CDOP model based on frequency scaling still contains some limitations that need to be corrected.

References

[1] C. Chen, S. Shiotani, and K. Sasa, "Effect of ocean currents on ship navigation in the east China sea," *Ocean Eng.*, vol. 104, pp. 283–293, Aug. 2015.

[2] J. Fischer and N. C. Flemming, *Operational Oceanography: Data Requirements Survey*. Southampton, U.K.: Southampton Oceanogr. Centre, 1999.

[3] A. Morang and L. T. Gorman, "Monitoring coastal geomorphology," in *Encyclopedia of Coastal Science*, M. L. Schwartz, Ed. Berlin, Germany: Springer-Verlag, 2005.

[4] D. M. Fratantoni, "North Atlantic surface circulation during the 1990s observed with satellite-tracked drifters," *J. Geo-Phys. Res.: Oceans*, vol. 106, no. C10, pp. 22067–22094, Oct. 2001.

[5] C. M. Senet, J. Seemann, and F. Ziemer, "The near-surface current velocity determined from image sequences of the sea surface," *IEEE Trans. Geosci. Remote Sens.*, vol. 39, no. 3, pp. 492–505, Mar. 2001, doi: 10.1109/36.911108.

[6] R. Gangeskar, "Ocean current estimated from X-band radar sea surface, images," *IEEE Trans. Geosci. Remote Sens.*, vol. 40, no. 4, pp. 783–792, Apr. 2002, doi: 10.1109/TGRS.2002.1006346.

[7] D. Barrick, "First-order theory and analysis of MF/HF/VHF scatter from the sea," *IEEE Trans. Antennas Propag.*, vol. AP-20, no. 1, pp. 2–10, Jan. 1972, doi: 10.1109/TAP.1972.1140123.

[8] D. R. Thompson, H. C. Graber, and R. E. Carande, "Measurements of ocean currents with SAR interferometry and HF radar," in *Proc. IEEE Int. Geosci. Remote Sens. Symp.*, 1994, vol. 4, pp. 2020–2022, doi: 10.1109/IGARSS.1994.399641.

[9] R. J. Martin and M. J. Kearney, "Remote sea current sensing using HF radar: An autoregressive approach," *IEEE J. Ocean. Eng.*, vol. 22, no. 1, pp. 151–155, Jan. 1997, doi: 10.1109/48.557549.

[10] C. Wunsch and E. M. Gaposchkin, "On using satellite altimetry to determine the general circulation of the oceans with application to geoid improvement," *Rev. Geophys.*, vol. 18, no. 4, pp. 725–745, Nov. 1980.

[11] N. Ducet, P. Y. LeTraon, and G. Reverdin, "Global high-resolution mapping of ocean circulation from the combinationof TOPEX/POSEIDON and ERS-1/2," *J. Geo-Phys. Res.: Oceans*, vol. 105, no. C8, pp. 19477–19498, Aug. 2000.

[12] B. Chapron, F. Collard, and F. Ardhuin, "Direct measurements of ocean surface velocity from space: Interpretation and validation," *J. Geo-Phys. Res.: Oceans*, vol. 110, no. C7, pp. 691–706, Jul. 2005.

[13] R. Romeiser, "The future of SAR-based oceanography: High-resolution current measurements by along-track interferometry," *Oceanography*, vol. 26, no. 2, pp. 92–99, Oct. 2013.

[14] A. Elyouncha, L. E. B. Eriksson, R. Romeiser, and L. M. H. Ulander, "Empirical relationship between the Doppler centroid derived from X-band spaceborne InSAR data and wind vectors," *IEEE Trans. Geosci. Remote Sens.*, vol. 60, 2022, Art. no. 4201120, doi: 10.1109/TGRS.2021.3066106.

[15] B. Sun, Y. Zhou, T. Li, and C. Guo, "Fast focused imaging algorithm for circular scanning SAR," *J. Beijing Univ. Aeronaut. Astronaut.*, vol. 33, no. 7, pp. 803–806, 2007.

[16] G. Yesheng, *Research on Imaging Algorithm of Circular Scanning Synthetic Aperture Radar*. Nanjing, China: Nanjing Univ. Aeronaut. Astronaut., 2007.

[17] Q. Bao, X. Dong, D. Zhu, S. Lang, and X. Xu, "The feasibility of ocean surface current measurement using pencil-beam rotating scatterometer," *IEEE J. Sel. Topics Appl. Earth Observ. Remote Sens.*, vol. 8, no. 7, pp. 3441–3451, Jul. 2015, doi: 10.1109/JSTARS.2015.2414451.

[18] Q. Bao, M. Lin, Y. Zhang, X. Dong, S. Lang, and P. Gong, "Ocean surface current inversion method for a Doppler scatterometer," *IEEE Trans. Geosci. Remote Sens.*, vol. 55, no. 11, pp. 6505–6516, Nov. 2017, doi: 10.1109/TGRS.2017.2728824.

[19] Q. Bao, Y. Zhang, M. Lin, and P. Gong, "An ocean current inversion accuracy analysis based on a Doppler spectrum model," *Acta Oceanologica Sinica*, vol. 36, pp. 101–107, Sep. 2017.

[20] E. Rodríguez et al., "Estimating ocean vector winds and currents using a Ka-band pencil-beam Doppler scatterometer," *Remote Sens.*, vol. 10, no. 4, Mar. 2018, Art. no. 576, doi: 10.3390/rs10040576.

[21] SKIM Team, "The SKIM team Sea surface KInematics Multiscale monitoring, full proposal for ESA EE9," 2017, doi: 10.13140/RG.2.2.16398.87365.

[22] SKIM Team, "ESA SKIM-MPRC-TN1 SKIM-MPRC TN-1: Science applications of the SKIM mission," 2019, doi: 110.13140/RG.2.2.28532.60802/3.

[23] F. Ardhuin et al., "SKIM, a candidate satellite mission exploring global ocean currents and waves," *Front. Mar. Sci.*, vol. 6, Apr. 2019, Art. no. 209.

[24] X. Dong, D. Zhu, W. Lin, H. Liu, and J. Jiang, "A Ku-band rotating fan-beam scatterometer: Design and performance simulations," in *Proc. IEEE Int. Geosci. Remote Sens. Symp.*, 2010, pp. 1081–1084, doi: 10.1109/IGARSS.2010.5650797.

[25] X. Dong, D. Zhu, W. Lin, H. Liu, and J. Jiang, "Status and recent progresses of development of the scatterometer of CFOSAT," in *Proc. IEEE Int. Geosci. Remote Sens. Symp.*, 2011, pp. 961–964, doi: 10.1109/IGARSS.2011.6049292.

[26] D. Entekhabi et al., "The soil moisture active passive (SMAP) mission," *Proc. IEEE*, vol. 98, no. 5, pp. 704–716, May 2010.

[27] X. Pan, G. Liao, Z. Yang, and H. Dang, "Sea surface current estimation using airborne circular scanning SAR with a medium grazing angle," *Remote Sens.*, vol. 18, no. 2, Jan. 2018, Art. no. 178, doi: 10.3390/rs10020178.

[28] X. Yao, X. Wang, L. Liu, S. Liu, X. Su, and H. Huang, "A platform errors estimation method based on radar echo for spaceborne Doppler scatterometer," *IEEE Trans. Aerosp. Electron. Syst.*, to be published, doi: 10.1109/TAES.2023.3261305.

[29] Y. Y. Yurovsky, V. N. Kudryavtsev, S. A. Grodsky, and B. Chapron, "Sea surface Ka-band Doppler measurements: Analysis and model development," *Remote Sens.*, vol. 11, no. 7, Apr. 2019, Art. no. 839.

[30] D. R. Thompson, "Calculation of microwave Doppler spectra from the sea surface with a time-dependent composite model," in *Proc. Radar Scattering From Modulated Wind Waves*. Berlin, Germany: Springer-Verlag, 1989, pp. 27–40.

[31] J. Wu, "Sea-surface drift currents induced by wind and waves," *J. Phys. Oceanogr.*, vol. 13, no. 8, pp. 1441–1451, Aug. 1983.

[32] F. Ardhuin, L. Marié, N. Rascle, P. Forget, and A. Roland, "Observation and estimation of Lagrangian, Stokes, and Eulerian currents induced by wind and waves at the sea surface," *J. Phys. Oceanogr.*, vol. 39, no. 11, pp. 2820–2838, Nov. 2009.

[33] F. Collard, A. Mouche, B. Chapron, C. Danilo, and J. Johannessen, "Routine high resolution observation of selected major surface currents from space," in *Proc. Adv. SAR Oceanogr. ENVISAT ERS Missions (SEASAR)*, 2008, vol. 21, Art. no. 25.
[34] A. A. Mouche et al., "On the use of Doppler shift for sea surface wind retrieval from SAR," *IEEE Trans. Geosci. Remote Sens.*, vol. 50, no. 7, pp. 2901–2909, Jul. 2012, doi: 10.1109/TGRS.2011.2174998.
[35] A. C. H. Martin, C. P. Gommenginger, and Q. Yves, "Simultaneous sea surface current and wind vectors retrieval with squinted SAR interferometry: Geophysical inversion and performance assessment," *Remote Sens. Environ.*, vol. 216, pp. 798–808, Oct. 2018.
[36] A. C. H. Martin, C. Gommenginger, J. Marquez, S. Doody, V. Navarro, and C. Buck, "Wind-wave induced velocity in ATI SAR sea surface currents: First experimental evidence from an airborne campaign," *J. Geo-Phys. Res.: Oceans*, vol. 121, no. 3, pp. 1640–1653, Mar. 2016.
[37] F. Fois, P. Hoogeboom, F. L. Chevalier, and A. Stoffelen, "An analytical model for the description of the full polarimetric sea surface Doppler signature," *J. Geo-Phys. Res.: Oceans*, vol. 120, no. 2, pp. 988–1015, Feb. 2015.
[38] Y. Miao, X. Dong, Q. Bao, and D. Zhu, "Perspective of a Ku-Ka dual-frequency scatterometer for simultaneous wide-swath ocean surface wind and current measurement," *Remote Sens.*, vol. 10, 2018, Art. no. 1042.
[39] T. Xiang, D. Zhu, and Y. Li, "Processing of circular-scanning SAR data using deramping-based imaging approach," *IEEE Geosci. Remote Sens. Lett.*, vol. 18, no. 4, pp. 657–661, Apr. 2021.
[40] R. Bamler, "Doppler frequency estimation and the Cramer-Rao bound," *IEEE Trans. Geosci. Remote Sens.*, vol. 29, no. 3, pp. 385–390, May 1991.
[41] W. Yu and Z. Zhu, "Comparison of Doppler centroid estimation methods in SAR," in *Proc. IEEE Aerosp. Electron. Conf.*, 1997, vol. 2, pp. 1015–1018, doi: 10.1109/NAECON.1997.622769.
[42] K. Miller and M. Rochwarger, "A covariance approach to spectral moment estimation," *IEEE Trans. Inf. Theory*, vol. IT-18, no. 5, pp. 588–596, Sep. 1972, doi: 10.1109/TIT.1972.1054886.
[43] J. Yu, "Accurate geometric positioning of high resolution satellite remote sensing imagery," Ph.D. dissertation, Dept. Elect., Wuhan Univ., Wuhan, China, 2009.

Xiaonan Yao was born in Shandong, China. She received the B.S. degree in electronic information science and technology from Yunnan University, Kunming, China, in 2016, and the M.Eng. degree in signal and information processing from the University of Chinese Academy of Sciences, Beijing, China, in 2019.

Since 2019, she has been with Sun Yat-sen University, Shenzhen, China. Her research interests include ocean remote sensing and signal processing for circular scanning SAR.

Xiaoqing Wang was born in Jiangxi, China, in 1978. He received the B.S. degree in electronic engineering from Xiamen University, Xiamen, China, in 2000, and the Ph.D. degree in signal and information processing from the University of Chinese Academy of Sciences, Beijing, China, in 2005.

From 2005 to 2016, he was an Assistant Researcher and Associate Researcher with the Institute of Electronics, Chinese Academy of Sciences. From 2016 to 2019, he was an Associate Researcher and Researcher with the Institute of Microelectronics, Chinese Academy of Sciences. Since 2019, he has been a Professor with the School of Electronics and Communication, Sun Yat-sen University, Shenzhen, China. His research interests include ocean microwave remote sensing, SAR signal processing, and radar processing.

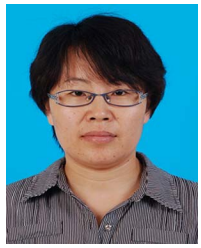

Lixia Liu received the M.D. degree in communication and information systems from the China Academy of Space Technology, Xi'an, China, in 2003.

From 2005 to 2012, she was responsible for the development of HY-2A Satellite microwave scatterometer of China as the Deputy Chief Designer. From 2010 to 2022, she was responsible for the development of FY-3E Satellite microwave scatterometer of China as the Chief Designer. Her research interests include system design of microwave remote sensing instrument, signal processing method research of radar, and system feasibility study of new microwave remote sensor.

Shubo Liu was born in Inner Mongolia Autonomous Region, China. She received the Ph.D. degree in physical oceanography from the Institute of Oceanology, Chinese Academy of Sciences, Qingdao, China, in 2015.

Her research interests include active and passive microwave remote sensing, geophysical parameters retrieval, and microwave emissivity model.

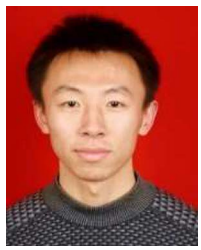

Xiang Su was born in Yunnan, China, in 1986. He received the B.S. degree in applied physics and the Ph.D. degree in radio physics from Xidian University, Xi'an, China, in 2009 and 2016, respectively.

He is currently a Senior Engineer with the China Academy of Space Technology, Xi'an, China. His research interests include electromagnetic scattering models, remote-sensing mechanism, retrieval, and high-performance computing for remote sensing.

Haifeng Huang received the B.S. degree in mathematics and the Ph.D. degree in information and communication engineering from the National University of Defense Technology, Changsha, China, in 1997 and 2005, respectively.

Since 2018, he has been a Professor and an Associate Dean of the School of Electronics and Communication Engineering, Sun Yat-sen University, Shenzhen, China. His research interests include basic theory and key technology in the field of space electronics and intelligent sensing and are mainly oriented toward intelligent remote sensing, surveying, oceanography, surveillance, geological hazards, and other applications.

Zheng Lu (Senior Member, IEEE) received the B.S. degree in information engineering and the Ph.D. degree in target detection and recognition from the Beijing Institute of Technology, Beijing, China, in 2008 and 2013, respectively.

He is currently a Senior Engineer with the Institute of Remote Sensing Satellite, China Academy of Space Technology, Xi'an, China. He is also the Program Manager of the Spaceborne Bistatic SAR Team. His research interests include spaceborne radar systems and signal processing (particularly synthetic aperture radar and pulse Doppler radar). In these research fields, he is also the Principal Investigator and an important participant in more than 20 grants and funding from different National or Governmental sources, including the National Natural Science Foundation of China, the Management Office of the Major Project of the High-Resolution Earth Observation System, the Beijing Municipal Science and Technology Commission, and the Administrative Commission of Zhongguancun Science Park.